

# Thermal instability in rotating shallow water with horizontal temperature/density gradients

É. Gouzien,<sup>1</sup> N. Lahaye,<sup>2</sup> V. Zeitlin,<sup>1,a)</sup> and T. Dubos<sup>3</sup>

<sup>1</sup>LMD, Ecole Normale Supérieure and University Pierre and Marie Curie, 24 rue Lhomond, 75005 Paris, France

<sup>2</sup>LOPS, IUEM, University of Western Brittany, rue Dumont d'Urville, 29280 Plouzané, France

<sup>3</sup>LMD, Ecole Polytechnique, 91128 Palaiseau, France

(Received 20 July 2017; accepted 28 September 2017; published online 12 October 2017)

A specific instability of vortices is found in rotating shallow water equations with horizontal density/temperature gradients, which is used for modelling atmospheric and oceanic mixed layers. The model is re-interpreted as dynamics of rotating non-isentropic two-dimensional gas. The instability, which was not reported previously, develops in a way suggesting its convective character. It appears when anomaly of buoyancy at the center of the vortex and the vorticity have opposite signs (for positive Coriolis parameters), and coexists with the standard barotropic instability, having higher growth rates in a wide range of parameters and leading to efficient mixing at a nonlinear stage. *Published by AIP Publishing.* <https://doi.org/10.1063/1.4996981>

Rotating shallow water (RSW) model is a classical conceptual model in geophysical fluid dynamics, allowing us to understand by simple means most of the dynamical phenomena taking place in the atmosphere and ocean at large scales, e.g., Ref. 1. A drawback of the model is that it does not admit horizontal temperature/density gradients. An extension of the model allowing for such gradients was repeatedly rediscovered in the literature both in the atmospheric and oceanic context<sup>2–6</sup> and can be conveniently called (rotating) thermal shallow water, TSW.<sup>7</sup> It was applied, in particular, to studies of well-mixed boundary layer in the ocean and in the atmosphere. The equations of the model can be obtained along the same lines as standard RSW, by vertical averaging of the primitive equations in the Boussinesq approximation, and hypothesis of columnar motion (mean-field approximation), but relaxing the hypothesis of uniform density/temperature, and read

$$\partial_t \mathbf{v} + \mathbf{v} \cdot \nabla \mathbf{v} + f \hat{\mathbf{z}} \wedge \mathbf{v} = -b \nabla h - \frac{h}{2} \nabla b, \quad (1)$$

$$\partial_t h + \nabla \cdot (\mathbf{v} h) = 0, \quad (2)$$

$$\partial_t b + \mathbf{v} \cdot \nabla b = 0. \quad (3)$$

Here  $\mathbf{v}$  is the two-dimensional velocity of the fluid column,  $h$  is its thickness, and  $b$  is the buoyancy related to density  $\rho$  in the oceanic context  $b = g\rho/\rho_0$ . The standard RSW equations are recovered in the limit of constant density  $\rho = \rho_0 = \text{const}$ . In the atmospheric context, density should be replaced by potential temperature with opposite signs.

We show below that this seemingly innocuous extension of the standard RSW leads to drastic changes in stability properties of stationary solutions. But first we would like to emphasise a fact which was apparently unnoticed in the literature. It is well-known that the standard RSW is equivalent to dynamics of a 2-dimensional isentropic gas with density  $h$

and the equation of state for pressure  $P = g \frac{h^2}{2}$ , in the presence of the Coriolis force. Similarly, (1)–(3) can be interpreted as dynamics of a 2-dimensional gas with density  $h$ , entropy  $b$ , and the equation of state  $P = \frac{bh^2}{2}$ .

We are interested in stability properties of stationary solutions of (1)–(3), which obey the “thermo-geostrophic” balance equations

$$f \hat{\mathbf{z}} \wedge \mathbf{v} = -b \nabla h - \frac{h}{2} \nabla b, \quad (4)$$

which can be re-interpreted as geostrophic balance of compressible gas:  $f \hat{\mathbf{z}} \wedge \mathbf{v} = -\frac{1}{h} \nabla P$ . This is unusual because in the so-called “primitive” equations in atmosphere and ocean dynamics the geostrophic balance is always considered in the context of (effectively) incompressible fluid. We limit ourselves here by stationary vortices characterised by radial distributions of  $h$ ,  $b$ , and azimuthal velocity  $v$ . We introduce typical spatial and velocity scales  $L$  and  $U$ , the value of unperturbed thickness of the fluid layer  $H_0$ , and a reference value of buoyancy  $b_0$ . The vortex solution is then characterised by Rossby and Burger numbers,  $Ro = U/fL$  and  $Bu = b_0 H_0 / f^2 L^2$ . We use the quasi-geostrophic scaling:  $v \sim U$ ,  $h \sim H_0 (1 + (Ro/Bu)H)$ ,  $b \sim b_0 (1 + 2(Ro/Bu)B)$ , assuming that all terms in (4) are of the same order. For non-dimensional azimuthal velocity  $V(r)$  and thickness and buoyancy distributions  $H(r)$  and  $B(r)$  of a stationary vortex in thermo-cyclogeostrophic balance, which replaces (4) for axisymmetric stationary solutions, we have

$$\left(1 + Ro \frac{V}{r}\right) V = \left(1 + 2 \frac{Ro}{Bu} B\right) H' + \left(1 + \frac{Ro}{Bu} H\right) B', \quad (5)$$

where prime denotes the derivative with respect to  $r$ . [Note that  $H(r)$  and  $B(r)$  here represent deviations from the values of respective fields at infinity.] As follows from (5), a given  $V(r)$  may be obtained from different  $H(r)$  and  $B(r)$ . We choose to work with a one-parameter family of solutions of (5) with buoyancy being proportional to the thickness of the isentropic (non-thermal) solution,

<sup>a)</sup>zeitlin@lmd.ens.fr

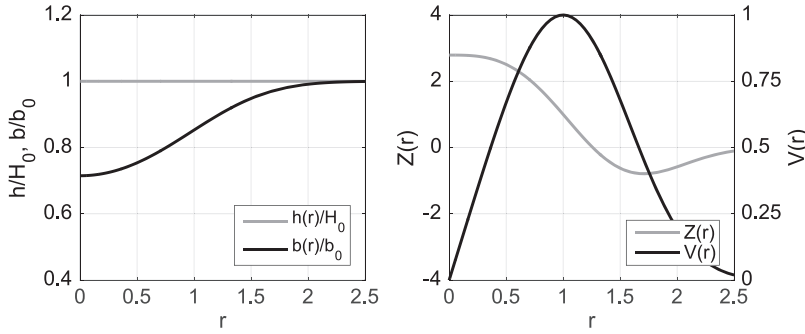


FIG. 1. Profiles of thickness  $h/H_0$  and density/potential temperature  $b/b_0$  (left panel) deviations, and velocity  $V$  and vorticity  $Z$  (right panel) of the localised vortex solution with  $\alpha = 0$ ,  $\beta = 3$ , and  $Ro = 0.1$ ,  $Bu = 1$ .

$$B(r) = (\alpha - 1) \int_r^\infty (1 + RoV/r')Vdr', \quad (6)$$

where  $\alpha$  is a parameter.  $H$  is then found from (5),

$$H(r) = \frac{\alpha}{1 - \alpha} \frac{Bu}{Ro} \left( 1 - \frac{1}{\sqrt{1 + 2\frac{Ro}{Bu}B}} \right). \quad (7)$$

When  $\alpha = 1$ , the solution of standard RSW equations is recovered by taking the corresponding limit in (5) and (6). We work with velocity profiles of the form  $V = r \exp(-(r^\beta - 1)/\beta)$ , where the parameter  $\beta$  controls the steepness. We present below the results of linear stability analysis, focusing on a purely thermal cyclonic vortex with  $\alpha = 0$ ,  $\beta = 3$ ,  $Ro = 0.1$ , and  $Bu = 1$ , which is displayed in Fig. 1. The linear stability analysis of the vortex solution goes along the standard lines: Equations (1)–(3) are linearised about the background vortex profile, the solutions of the linearised problem are sought in form of Fourier-modes in azimuthal angle  $\phi$  and time  $\propto e^{i(l\phi - \omega t)}$ , and the resulting system of ordinary differential equations in  $r$  is solved by using a pseudo-spectral collocation method.<sup>8</sup> The dependence of the imaginary part (growth rate), and of the real part divided by  $l$  (phase velocity) of the eigenfrequencies found in this way, as functions of  $l$ , is presented in Fig. 2. It should be stressed that a vortex with the same

velocity profile in standard RSW is unstable with respect to the classical barotropic instability. This instability is recovered in our analysis at  $\alpha = 1$  and has the azimuthal wavenumber  $l = 2$ . It exists at any  $\alpha$  with roughly the same characteristics (asterisk in Fig. 2). However, surprisingly, a whole spectrum of new unstable modes appears for all  $l$  with the most unstable mode with  $l = 5$  and the growth rate substantially higher than that of the barotropic instability. Moreover, the growth rate of the new instability, which we will call thermal, with the same wavenumber  $l = 2$  as the barotropic instability is higher.

The radial structure of the thermal instability mode with  $l = 5$  having the highest growth rate is presented in Fig. 3. The radial structure of unstable modes with different  $l$  is similar (not shown). For each  $l$ , a spectrum of unstable modes with growth rates decreasing with a number of nodes in the radial direction exists (it is shown only for  $l = 5$  in Fig. 2). As follows from Fig. 3, the unstable mode is localised in the vicinity of the critical level  $r_c$ , such that the phase velocity of the wave (the real part of the eigenfrequency divided by  $l$ ) is equal to  $V(r_c)$ . Another remarkable feature of the obtained dispersion curves is that there is a well defined maximum of the growth rate as a function of  $l$ , and that the eigen-phase velocities saturate with increasing  $l$ . Two-dimensional structure of the most unstable mode is presented in Fig. 4, left panel, in terms of vorticity.

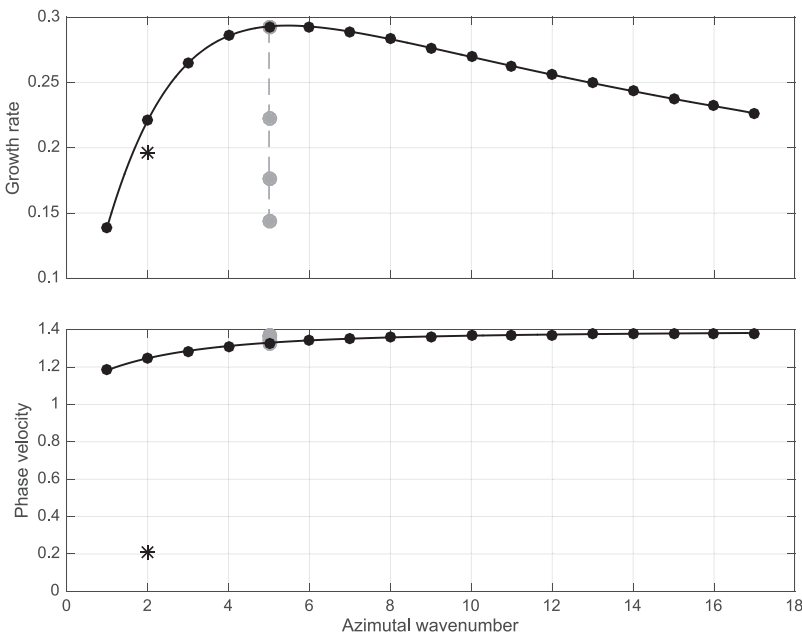


FIG. 2. Growth rate (upper panel) and phase velocity (lower panel) of the unstable modes as functions of azimuthal wavenumber  $l$ . Asterisk—standard barotropic instability (only the most unstable mode is shown). Circles—new instability: black—most unstable modes at each  $l$ , gray—unstable modes with a higher number of nodes in the radial direction (shown only for  $l = 5$ ). Upper panel reprinted with permission from Gouzien *et al.*, “Instabilities of vortices and jets in thermal rotating shallow water model,” in *Proceedings of International Conference on Topical Problems of Fluid Mechanics*, pp. 147-152 (2017). Copyright 2017, Institute of Thermomechanics.

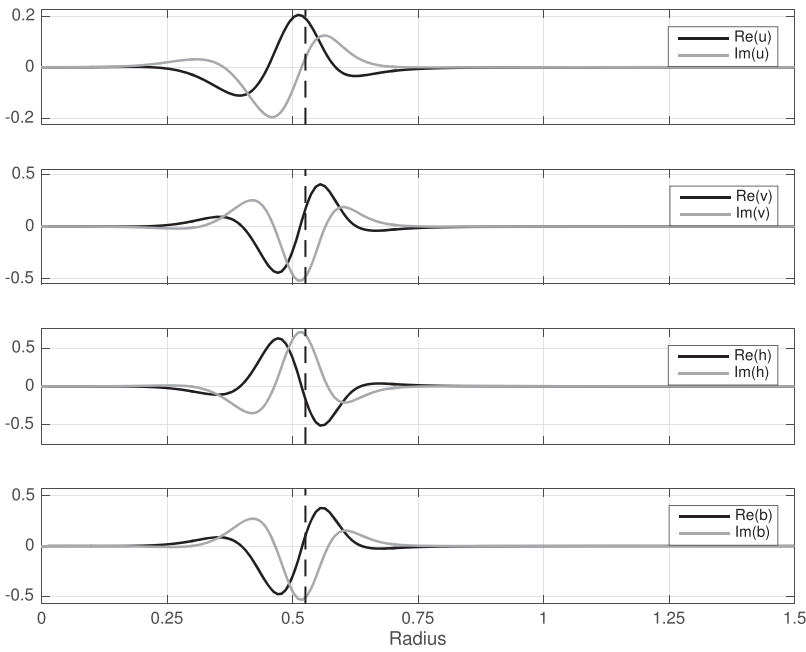


FIG. 3. Radial profiles of all components of the leading unstable mode  $l = 5$ . Dashed line: position of the critical level. Reprinted with permission from Gouzien *et al.*, “Instabilities of vortices and jets in thermal rotating shallow water model,” in *Proceedings of International Conference on Topical Problems of Fluid Mechanics*, pp. 147-152 (2017). Copyright 2017, Institute of Thermomechanics.

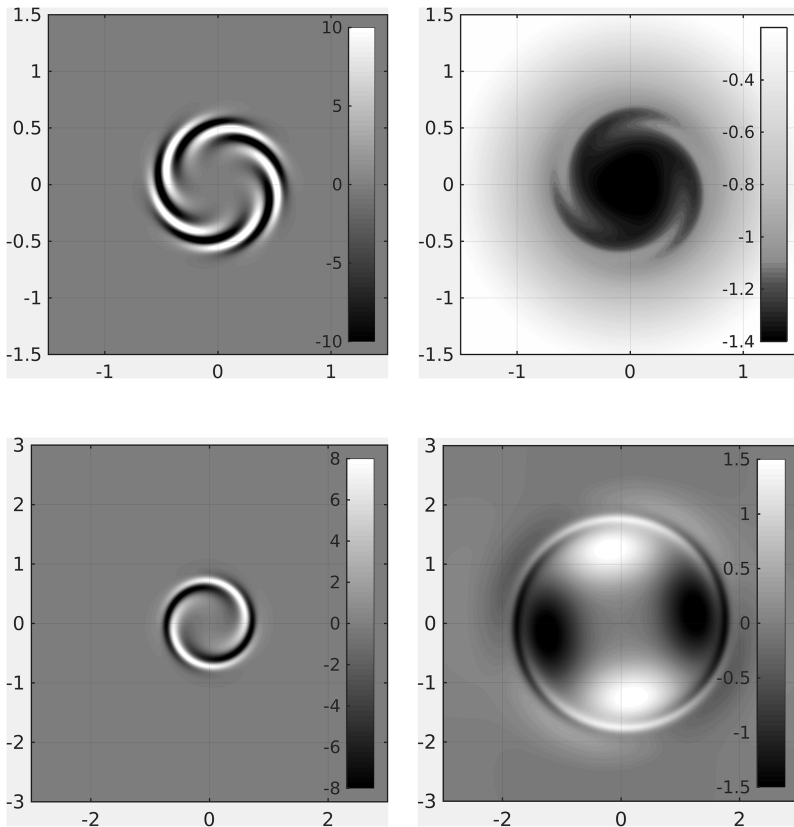


FIG. 4. Vorticity distribution in the  $x$ - $y$  plane [spatial extent:  $(-1.5, 1.5)$ ] in the leading unstable mode  $l = 5$  (left), and buoyancy field (unstable mode superimposed to the background state with relative amplitude 0.1) in the  $l = 3$  unstable mode (right). The latter corresponds to the initial conditions for the numerical simulation of nonlinear saturation.

FIG. 5. Vorticity distribution in the  $x$ - $y$  plane [spatial extent:  $(-3, 3)$ ] in the unstable mode with  $l = 2$  of the thermal (left) and barotropic (right) instabilities. Reprinted with permission from Gouzien *et al.*, “Instabilities of vortices and jets in thermal rotating shallow water model,” in *Proceedings of International Conference on Topical Problems of Fluid Mechanics*, pp. 147-152 (2017). Copyright 2017, Institute of Thermomechanics.

Distributions of buoyancy perturbation are similar. The structure of modes with different  $l$  is of the same type, with corresponding decrease of the azimuthal wavelength.

To emphasize the difference between the barotropic and thermal instabilities, we present in Fig. 5 a comparison of the horizontal structure of the barotropic and thermal instability modes with the same wavenumber, as seen in vorticity distribution. The radial structure of the barotropic instability mode is also different (not shown).

The thermal instability exists also for anticyclones, but has smaller growth rates at the same  $\alpha$ ,  $Ro$ , and  $Bu$ . We studied the dependence of the growth rates for both cyclones and anticyclones on the parameters  $\alpha$ ,  $Ro$ , and  $Bu$ . The results are shown in Fig. 6. For  $\alpha$  increasing from 0 to 1, the growth rates of the thermal instability of both cyclones and anticyclones are rapidly decreasing and vanish at  $\alpha = 1$ , while the growth rate of the barotropic instability decreases, but much slower, becoming dominant at  $\alpha \rightarrow 1$  (Fig. 6, left panel). At moderate

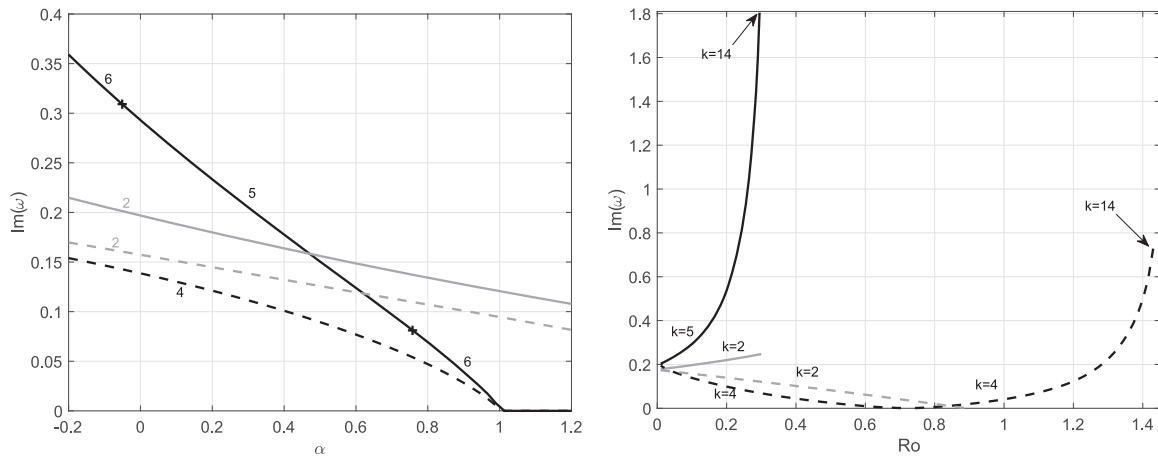


FIG. 6. *Left*: Dependence on  $\alpha$  of the growth rates of most unstable thermal and barotropic modes of cyclonic and anticyclonic vortices with  $Ro = 0.1$  and  $Bu = 1$ . Changes of the azimuthal structure of the most unstable mode are marked by crosses. *Right*: Dependence of growth rates of the most unstable thermal and barotropic modes on the Rossby number. Curves terminate if drying ( $h \rightarrow 0$ ) occurs in the mean vortex profile. On both panels: solid—cyclone, dashed—anticyclone; black—thermal mode, grey—barotropic mode. Wavenumbers of the most unstable modes are indicated by numbers.

Rossby numbers, barotropic instability is dominant for anticyclones at all  $\alpha$ , while for cyclones there is a swap of dominant instabilities at  $\alpha \approx 0.44$ , the thermal instability being stronger at smaller  $\alpha$  (Fig. 6, left panel). We investigated the sensitivity of the instability to the values of  $Ro$  between 0.01 and 0.35 (Fig. 6, right panel) and  $Bu$  between 0.1 and 10. While the growth rate of the barotropic instability remains roughly constant under our scaling, the growth rate of the thermal modes increases with increasing  $Ro$  and/or decreasing  $Bu$ . The growth rates of the thermal instability of cyclones increase very rapidly with the Rossby number, especially in the vicinity of the value corresponding to drying (Fig. 6, right panel). For anticyclones, however, they first decrease and reach a minimum when the Coriolis and the centrifugal forces cancel each other near the center of the vortex, resulting in flattening of the buoyancy profile in this region (for larger values of the Rossby number, the radial derivative of buoyancy is positive at the center of the vortex). This explains the strong asymmetry between cyclones and anticyclones already observed in the left panel of Fig. 6, as centrifugal and Coriolis forces add up in cyclones, instead of compensating each other. We also checked the sensitivity of the growth rates to the steepness of the vortex profile by varying  $\beta$  between 2 (Gaussian profile) and 4. The growth rate of the thermal instability at any  $l$  decreases with decreasing  $\beta$ . At  $l = 2$ , it falls below the growth rate of the barotropic instability at  $\beta \approx 2.2$ .

In order to illustrate nonlinear saturation of the instability, we show in Fig. 7 snapshots of nonlinear evolution of an initially purely thermal vortex with  $\alpha = 0$ , as seen in the buoyancy field. A number of numerical simulations of developing instability were done at different Rossby numbers, typically between 0.01 and 0.1, both for cyclones and anticyclones, and gave qualitatively similar results. The example we present corresponds to a cyclone with  $Ro = 0.1$  and  $Bu = 1$ . To perform the simulations, a second-order centered finite-difference shallow-water scheme<sup>9</sup> was extended to TSW by adding the corresponding terms in the momentum equations and an upwind-biased finite-volume buoyancy transport scheme. An explicit minimal Newtonian viscosity was added in the equations of

the model to inhibit development of numerical instabilities. A mode  $l = 3$  was superimposed, with a small amplitude (this perturbation is practically invisible in the first panel of the figure), onto the vortex at the initial moment. As follows from the figure, the amplitude of the perturbation grows, maintaining the pattern corresponding to the unstable mode. The growth rate matches the prediction of the linear stability analysis (not shown), and the structure of the developing instability at the linear stage (upper right panel in Fig. 7) matches very well the one of the linearly unstable mode (cf. Fig. 4, right panel). Nonlinear saturation of the instability reveals typical convective patterns and leads at late stages to a strong mixing of the buoyancy field, although buoyancy anomaly does not totally disappear. It is worth noting that a negative anomaly of thickness appears due to this process (not shown).

The thermal instability of vortices in TSW was, apparently, not reported previously. It appears for warm-core (in a sense that diminished density is related to a positive temperature anomaly) cyclonic and cold-core anticyclonic vortices in the oceanic context, and cold (warm)-core cyclones (anticyclones) in the atmospheric one, and induces effective mixing during nonlinear evolution. The thermal instability thus provides a mechanism for dissipating certain coherent structures, while not affecting others, e.g., in the mixed layer in the ocean and atmosphere, where the model was applied previously. It should be stressed that although we presented results for vortex instabilities, similar instabilities arise for jets. In particular, we confirmed a surprising instability of uniform-velocity flow in a channel, which was discovered in Refs. 10 and 11. In the last paper, a comparison of TSW results with simulations with a continuously stratified model gave indications on the link of the new instability with symmetric instability,<sup>12</sup> which is, in fact, a variant of essentially ageostrophic baroclinic instability. In the case of vortices, the instabilities we discovered are, probably, also related to essentially ageostrophic baroclinic instabilities, like the asymmetric centrifugal one.<sup>13</sup> The resemblance of the most unstable modes of Fig. 3 with unstable modes of asymmetric centrifugal instability found in Ref. 13 is striking. There is also a strong resemblance of the patterns of nonlinear

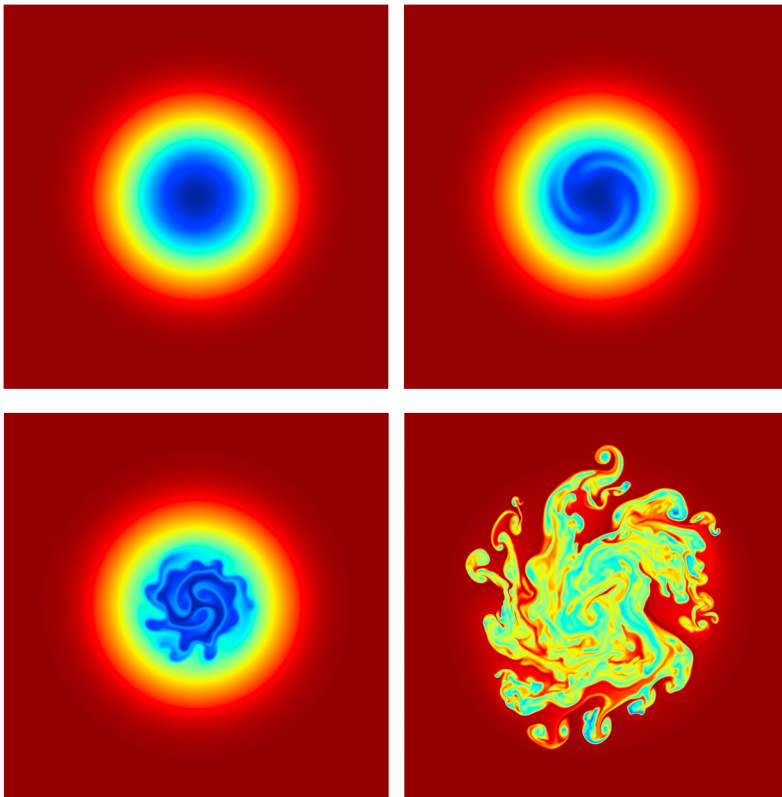


FIG. 7. Snapshots of the evolution of buoyancy during nonlinear saturation of the thermal instability.

saturation of Fig. 7 and that of ageostrophic instabilities of eddies in the mixed layer of the ocean obtained by direct numerical simulations.<sup>14</sup> This relation of the thermal instabilities of vortices in TSW to ageostrophic instabilities in the full primitive equations model needs further investigation. Let us finally mention that, as it was already discussed in early works, cf., e.g., Refs. 5 and 6, TSW has an obvious handicap: its stationary solutions do not respect the thermal wind balance. This happens because in the primitive equations horizontal gradients of density/temperature induce, through the hydrostatic balance, vertical variations of the horizontal pressure gradient, which are removed by imposing the mean-field approximation. We should remind that in the latter all averages of the products of different fields are replaced by products of averages. This may be corrected by introducing higher moments which compensate the above-mentioned imbalance, as discussed in Ref. 6. We should however stress that, in spite of this unusual property, the model is self-consistent, as is clear already from the gas dynamics analogy developed above.

Preliminary results of this work were published in Ref. 15.

<sup>1</sup>V. Zeitlin, “Fundamentals of rotating shallow water model in the geophysical fluid dynamics perspective,” in *Nonlinear Dynamics of Rotating Shallow Water: Methods and Advances*, Nonlinear Science and Complexity Vol. II, edited by V. Zeitlin (Springer, 2007), pp. 1–46.

<sup>2</sup>R. L. Lavoie, “A mesoscale numerical model of lake-effect storms,” *J. Atmos. Sci.* **29**, 1025–1040 (1972).

<sup>3</sup>M. L. Salby, “Deep circulations under simple classes of stratification,” *Tellus A* **41A**, 48–65 (1989).

<sup>4</sup>J. P. McCreary, P. K. Kundu, and R. L. Molinari, “A numerical investigation of dynamics, thermodynamics and mixed-layer processes in the Indian Ocean,” *Prog. Oceanogr.* **31**, 181–244 (1993).

<sup>5</sup>P. Ripa, “On improving a one-layer ocean model with thermodynamics,” *J. Fluid Mech.* **303**, 169–201 (1995).

<sup>6</sup>D. P. Dempsey and R. Rotunno, “Topographic generation of mesoscale vortices in mixed-layer models,” *J. Atmos. Sci.* **45**, 2961–2978 (1988).

<sup>7</sup>E. S. Warnerford and P. J. Dellar, “The quasi-geostrophic theory of the thermal shallow water equations,” *J. Fluid Mech.* **723**, 374–403 (2013).

<sup>8</sup>L. N. Trefethen, *Spectral Methods in MATLAB* (SIAM, 2000).

<sup>9</sup>R. Sadourny, “The dynamics of finite-difference models of the shallow-water equations,” *J. Atmos. Sci.* **32**, 680–689 (1975).

<sup>10</sup>W. R. Young and L. Chen, “Baroclinic instability and thermohaline alignment in the mixed layer,” *J. Phys. Oceanogr.* **25**, 3172–3185 (1995).

<sup>11</sup>Y. Fukamachi, J. P. McCreary, and J. A. Proehl, “Instability of density fronts in layer and continuously stratified models,” *J. Geophys. Res.* **100**, 2559–2577, doi:10.1029/94jc02656 (1995).

<sup>12</sup>P. Stone, “On non-geostrophic baroclinic instability,” *J. Atmos. Sci.* **23**, 390–400 (1966).

<sup>13</sup>N. Lahaye and V. Zeitlin, “Centrifugal, barotropic and baroclinic instabilities of isolated ageostrophic anticyclones in the two-layer rotating shallow water model and their nonlinear saturation,” *J. Fluid Mech.* **762**, 5–34 (2015).

<sup>14</sup>L. Brannigan, “Intense submesoscale upwelling in anticyclonic eddies,” *Geophys. Res. Lett.* **43**, 3360–3369, doi:10.1002/2016gl067926 (2016).

<sup>15</sup>E. Gouzien, N. Lahaye, V. Zeitlin, and T. Dubos, “Instabilities of vortices and jets in thermal rotating shallow water model,” in *Proceedings of International Conference on Topical Problems of Fluid Mechanics*, edited by D. Simurda and T. Bodnar (Institute of Thermomechanics, Prague, 2017), pp. 147–152.